Ru-RuO2 nano-heterostructures stabilized by the sacrificing oxidation strategy of Mn3O4 substrate for boosting acidic oxygen evolution reaction

Long, Xin; Zhao, Bin; Zhao, Qianqian; Wu, Xuexian; Zhu, Meng-Nan; Feng, Renfei; Shakouri, Mohsen; Zhang, Yu; Xiao, Xinxin; Zhang, Jiujun; Fu, Xian-Zhu; Luo, Jing-Li

Published in:
Applied Catalysis B: Environmental

DOI (link to publication from Publisher):
10.1016/j.apcatb.2023.123559

Publication date:
2024

Ru-RuO_2 nano-heterostructures stabilized by the sacrificing oxidation strategy of Mn_3O_4 substrate for boosting acidic oxygen evolution reaction

Xin Long[a], Bin Zhao[a,] *, Qianqian Zhao[a], Xuexian Wu[a], Mengnan Zhu[b], Renfei Feng[c], Mohsen Shakouri[c], Yu Zhang[d], Xinxin Xiao[e], Jiujun Zhang[f], Xian-Zhu Fu[a], Jing-Li Luo[a,] *

[a] Shenzhen Key Laboratory of Polymer Science and Technology, Guangdong Research Center for Interfacial Engineering of Functional Materials, College of Materials Science and Engineering, Shenzhen University, Shenzhen 518060, China.

[b] Department of Chemical and Materials Engineering, University of Alberta, Edmonton, Alberta T6G 2G6, Canada.

[c] Canadian Light Source Inc., Saskatoon, S7N 0X4, Saskatchewan, Canada.

[d] Instrumental Analysis Center of Shenzhen University (Lihu Campus), Shenzhen University, Shenzhen, Guangdong 518055, China.

[e] Department of Chemistry and Bioscience, Aalborg University, Fredrik Bajers Vej 7H, 9220 Aalborg East, Denmark.

[f] Institute for Sustainable Energy, College of Sciences, Shanghai University, Shanghai, 200444, China.

* Correspondence and requests for materials should be addressed to B.Z. (email: bin.zhao@szu.edu.cn) and J.-L. L. (email: jll@szu.edu.cn)

Abstract: Designing anodic electrocatalysts with high activity and robust stability for acidic oxygen evolution reaction (OER) is significant for the large-scale promotion of sustainable proton exchange membrane water electrolysis (PEMWE). Most reported Ru-based electrocatalysts tend to further improve activity at the expense of stability, herein, we report the synthesis of crystalline Mn_3O_4 supported Ru-RuO_2 nano-heterostructures as the anodic electrocatalyst that only requires a low overpotential of 182 mV (10 mA cm^{-2}) for acidic OER, accompanied with a record stability of 400 h in 0.5 M H_2SO_4. The results of XPS, ICP-MS, and XAS indicate that the Mn_3O_4 substrate plays a crucial role in greatly stabilizing Ru-RuO_2 nano-heterostructure by preventing Ru from over-oxidation and dissolution. Meanwhile, DEMS with isotope labeling reveals that the Ru-RuO_2 nano-heterostructure contributes to suppressing lattice oxygen oxidation mechanism (LOM) and concurrently expediting the involvement of adsorbate evolution mechanism (AEM) for boosting the acidic OER performance.

Keywords: acidic OER; Ru-based electrocatalysts; heterostructure; Mn_3O_4 substrate; stability.

1. Introduction

Electrochemical water splitting is broadly regarded as a promising and sustainable technique for producing green hydrogen, crucial to achieving the global mission of carbon neutrality [1]. Nowadays, the alkaline water electrolysis with a long research history has been equipped with a mature process route and is commercially available for producing hydrogen, but it still suffers from some fundamentally practical limitations, such as high ohmic resistance, low operational pressure, and the crossover of gases [2]. In contrast, employing a polymer-based proton exchange membrane under acidic medium, the well-known PEMWE has garnered extensive attention because it can effectively solve the above problem with markedly enhanced performance. Nevertheless, the large-scale deployment of PEMWE is widely hampered by the lack of acidic OER electrocatalysts with high activity, robust stability, and low cost [2, 3]. To date, RuO_2 is considered as the benchmark electrocatalyst for acidic OER but its inferior dissolution resistance makes it difficult to put into PEMWE commercial operation [4]. Although IrO_2 is more stable than RuO_2 in acidic media, the price of Ir is about 7.5 times higher than Ru [3]. Hence, IrO_2 is costly to serve as commercial anode electrocatalysts for PEMWE. Therefore, the elaborate design of Ru-based electrocatalysts to further enhance acidic OER performance and durability is highly imperative.

The thorough understanding of acidic OER reaction mechanism can provide insightful guidance for the design of rational electrocatalysts. There are two major mechanisms for acidic OER process of Ru-based electrocatalysts: the adsorbate evolution mechanism (AEM) and the lattice oxygen oxidation mechanism (LOM). The former generates routine OER intermediates (OH^*, O^*, and OOH^*) from the adsorbates (H_2O, in acidic medium) and exhibits a universal volcano relationship between catalytic activity and binding energy thermodynamically [5-7]; while the latter involves direct O-O coupling between the oxo-intermediates and lattice oxygen which is in favor of the OER kinetics process [8, 9]. It has been proposed that the low intrinsic activity and poor stability of rutile RuO_2 stems from the participation of lattice oxygen, leading to the collapse of catalytic structure and undermining the stability of Ru-based electrocatalysts in acid [10-12]. To accomplish stability in Ru-based electrocatalysts, it is necessary to accelerate the AEM pathway while inhibiting the involvement of the LOM pathway, which demands the design of Ru-based electrocatalysts with optimal surface energies for intermediates [13]. Moreover, excessive oxidation of Ru atoms at high overpotentials leads to high valence state $Ru^{\delta>4+}$ species which are beneficial for high acidic OER activity but are soluble. In consequence, the high activity of RuO_2 only remains few hours and then the Ru ions rapidly dissolve into the electrolyte [11, 14-16].

Recently, enormous efforts have been undertaken to develop advanced Ru-based electrocatalysts via various strategies including engineering heterostructures (Ru-RuO_2@NPC) [17], doping (Co-RuO_2) [18], strain effect (Ru_1-Pt_3Cu) [12], ultra-thin two-dimensional nanostructure (ultra-thin RuO_2 nanosheets) [19], solid-solution oxides ($Mn_{0.75}Ru_{0.25}O_{2-d}$) [20], and so on. Nevertheless, the stability of most Ru-based electrocatalysts reported so far is still unsatisfactory, not reaching industrial application requirements [21]. It is desirable to develop new strategies to achieve simultaneously both enhanced stability and activity for electrocatalysts. Recent literature revealed that constructing a RuO_2/CoO_x hybrid electrocatalyst could form a stable interface to prevent the excessive oxidation of RuO_2 and break the stability-activity seesaw relation on Ru-based electrocatalysts [22]. Experimental and theoretical calculations verify that the sacrificing oxidation is an avail strategy to simultaneously improve activity and stability. Meanwhile, the catalyst-support interaction also makes contributions to improving acidic OER performance, rational interfacial engineering plays a crucial role in creating new active sites and stabilizing components [22-24]. It is expected that the construction of a sacrificial substrate could effectively balance the catalytic activity and stability of high-valence $Ru^{\delta>4}$ species. Hence, utilizing earth-abundant and economical metals as substrate components can reduce the use of precious metal Ru and benefit sustainable development. Combining the sacrificing oxidation of substrate and heterostructure synergistic effect could be an effective strategy to simultaneously enhance both stability and activity in acidic OER, but such work is still challenging and rarely reported.

Herein, inspired by the above strategy, we report the crystalline Mn_3O_4 supported Ru-RuO_2 nano-heterostructures on carbon paper as the highly active and stable electrocatalyst under acidic condition. Ru-RuO_2/Mn_3O_4/CP exhibits a significantly high activity (only 182 mV at 10 mA cm^{-2} and 1324.6 A $g_{Ru}^{-1}$of mass activity at 1.50 V vs. RHE) and maintains outstanding long-term stability (400 h) under continuous operation in 0.5 M H_2SO_4. Besides, the anodic electrocatalyst Ru-RuO_2/Mn_3O_4/CP coupled with a commercial Pt/C (20 wt%) displays continuous water electrolysis for more than 65 h at 50 mA cm^{-2} in the practical PEM electrolyzer. X-ray photoelectron spectroscopy, Time-dependent elemental analysis, and X-ray absorption spectroscopy results reveal that the enhanced activity and stability of Ru-RuO_2/Mn_3O_4/CP can be ascribed to the sacrificing oxidation of Mn_3O_4 substrate, which is efficient to prevent the electrocatalyst from the over-oxidation and dissolution of Ru species for acidic OER. *Operando* differential electrochemical mass spectrometry (DEMS) with isotope labeling measurements confirms the formation of Ru-RuO_2 nano-heterostructures can suppress the LOM pathway during OER, leading to promoted OER stability and activity in acidic media.

2. Experimental

2.1. Materials and synthesis

Ruthenium (III) chloride hydrate ($RuCl_3.H_2O$, 98%), Ruthenium on carbon (Ru 5%, MW=101.07), Ruthenium (IV) oxide (99.9%), Polyvinylpyrrolidone (PVP10, MW=58000) were obtained from Macklin. Manganese (II) chloride tetrahydrate ($MnCl_2.4H_2O$, ≥99%), Nafion solution (~5% in a mixture of lower aliphatic alcohols and water) were obtained from

Sigma-Aldrich. Water-^{18}O ($H_2{}^{18}O$, 97 at% ^{18}O) were purchased from Energy Chemical. All reagents were used as received without further purification.

The Ru-RuO_2/Mn_3O_4/CP electrocatalyst was synthesized following the previously reported impregnation method with minor modifications [25]. Before deposition, commercial carbon paper (CP) was cut into pieces of 1 × 1.5 cm $^{-2}$ and respectively treated with acetone, hydro-chloric acid (1 M) and deionized water for 30 min under ultrasonic conditions to remove surface oily impurity and oxides. In a typical procedure, $RuCl_3.H_2O$ (0.7 mmol), $MnCl_2.4H_2O$ (0.7 mmol) and 160 mg PVP were dissolved into 5 mL deionized water (18.2 MΩ) and then stirred overnight before loading. The impregnation method was applied to directly synthesize electrode with catalysts in situ growing on the CP substrate. Specifically, the CP was impregnated into the precursor solution for 5 min and then dried in a vacuum oven at 60 °C. After drying for 20 min, the precursor modified CP was transferred into a muffle furnace and heated to 400 °C at 10 °C min $^{-1}$ in air atmosphere, and then held for 6 hours. Furthermore, the pristine Ru-RuO_2/CP (without Mn precursor) and Mn_3O_4/CP (without Ru precursor) were obtained separately with the same experimental procedure. The Ru-RuO_2/Mn_3O_4, Ru-RuO_2, and Mn_3O_4 electrocatalysts growing on carbon paper were directly used as the working electrode in the standard three-electrode system.

For the preparation of control group, 5 mg catalyst was dispersed in 950 μL mixture of water and ethanol (1:8.5, v/v), and then 50 μL of 5 wt % Nafion solution was added. The mixed solution was followed by ultrasonication for 30 min to obtain a homogeneous catalyst suspension. Afterwards, 100 μL catalyst ink was dropped on the carbon paper (loading area 1 × 1 cm $^{-2}$) yielding a mass loading of 0.5 mg cm^{-2}. The modified electrode (commercial RuO_2/CP and RuC/CP) was dried at ambient temperature before electrochemical measurements.

2.2. Catalyst characterization

The as-synthesized electrocatalysts were characterized by field-emission SEM images using Hitachi SU-70 system (probe current 100 nA, accelerating voltages 10 kV), which was equipped with Oxford INCA (Aztec) X-ray spectroscopy (EDS) detector at 20 kV to analyze composition. TEM、HRTEM and HAADF-STEM images were performed on JEOL JEM-F200 system (acceleration voltage 200 kV) equipped with a EDS detector at 20 kV.

To study the phase composition of the sediment on the carbon paper, the vacuum dried powder was taken for X-ray diffraction (XRD) test. XRD were recorded with a RIGAKU Smartlab using Cu Kα radiation (λ = 1.5406 Å). X-ray photoelectron spectroscopy (XPS) measurements were carried out on a Thermo Scientific ESCALAB 250Xi spectrometer. The K-edge X-ray Absorption Fine Structure (XAFS) of Ru and Mn elements for electrocatalysts were recorded by synchrotron radiation light source using a hard X-ray beam of "VESPERS" at Canadian Light Source (CLS), Canada. The loading of Ru and Mn on carbon paper and the dissolution of catalysts during OER process were quantified by ICP-MS (Agilent ICP-MS 7700).

2.3. Electrocatalytic methods and Fabrication of membrane electrode assembly

All the electrochemical measurements including Linear Sweep Voltammetry (LSV), Electrochemical impedance spectroscopy (EIS), Electrochemical double-layer capacitance (C_{dl}), and Faradaic efficiency (FE) for acidic OER were conducted on a CHI 760E electrochemical workstation (CH Instruments, Inc., Shanghai, China) at room temperature with a standard three-electrode system. These electrocatalytic methods and membrane electrode assembly (MEA) test were described in Supplementary data in detail.

2.4. Differential electrochemical mass spectroscopy (DEMS) measurements.

DEMS measurements were carried out using a QAS 100 device (Linglu Instruments, Shanghai). A saturated Ag/AgCl electrode and a Pt wire were used as reference electrode and counter electrode, respectively. The working electrodes were prepared by sputtering Au onto 50 μm thick porus PTFE films. Then, the catalysts were dropped and casted onto the Au film with a mass loading of 0.75 mg cm $^{-2}$. All samples were labeled with ^{18}O isotopes by performing 10 CV cycles at a scan rate of 5 mV s $^{-1}$ in 0.5 M H_2SO_4 using $H_2{}^{18}O$ as the solvent (All samples were scanned for LSV near the onset potential of OER). Afterward, the ^{18}O-labeled catalysts were rinsed with $H_2{}^{16}O$ for several times and dried to remove the residual $H_2{}^{18}O$ in order to avoid the interruption of surface adsorbed ^{18}O species to the observed $^{34}O_2$ ($^{16}O^{18}O$) MS signals. Finally, the cyclic CV scans were carried out in a normal 0.5 M H_2SO_4 solution at appropriate potential windows and scan rate. In the meantime, the gaseous products including $^{32}O_2$ ($^{16}O^{16}O$), $^{34}O_2$ ($^{16}O^{18}O$), and $^{36}O_2$ ($^{18}O^{18}O$) during OER process were measured in real time by mass spectroscopy. Before the electrochemical measurements, all the electrolytes were purged with high-purity Ar to remove the dissolved oxygen.

2.5. Computational details

All the spin-polarized DFT calculations are conducted based on the Vienna Ab-inito Simulation Package (VASP) [26, 27]. The electron-ion interactions are described by the Projected Augmented-Wave (PAW) potentials, while the exchange-correlation interactions are calculated by employing the Perdew-Burke-Enzerhof (PBE) functional of Generalized Gradient Approximation (GGA) with a Hubbard U extension (U value) of 3.9 eV, and 4.88 eV for Mn and Ru [28, 29]. The vdW-D3 method developed by Grimme was employed to describe the van der Waals interaction [30]. The Ru-RuO_2 heterostructure is built using RuO_2 (101) and Ru (100). The plane-wave energy cutoff is set as 450 eV. The convergence threshold is set as 1.0×10^{-5} eV in energy and 0.05 eV per Angstrom in force. A vacuum layer of 15 Å is adopted to avoid the periodic interactions. The Brillouin zone is modeled by gamma centered Monkhorst-Pack scheme, in which the 4×4×1 and 1×3×1 grids are adopted for RuO_2 (110) and Ru-RuO_2, respectively.

The change in the Gibbs free energy of each reaction is calculated as follow:

$$\Delta G=\Delta E_{pot}+\Delta E_{ZPE}-T\Delta S$$

in which the ΔE_{pot}, ΔE_{ZPE} and the ΔS are referred to as the change in potential energy, the change in the zero-point energy, and the change in the entropy.

The zero-point energy was calculated by the summation of all vibrational frequencies:

$$E_{\mathrm{ZPE}} = \frac{1}{2}\sum h\upsilon$$

where the ν corresponds to the vibrational frequency of each normal mode [31].

3.Results and discussion

2.1 Structural analysis

The electrocatalysts of Ru-RuO_2/Mn_3O_4/CP, Ru-RuO_2/CP, and Mn_3O_4/CP were synthesized in situ on carbon paper through an impregnation-calcination method based on a previous report, which was easily accessible for large-scale preparation [25]. The transmission electron microscopy (TEM) image in Fig. 1a obviously displays the anisotropic lattice fringes of the three phases in Ru-RuO_2/Mn_3O_4/CP, notably, the magnified TEM image of Fig. 1b presents Ru (100) and RuO_2 (110) heterostructures loaded on Mn_3O_4 (112) exhibit plentiful defects (marked by the white dashed lines). The nano-heterostructures exposed on the surface of the electrocatalyst are helpful to increase the lattice defects, which subsequently produce abundant active sites to promote electrocatalytic activity and it is easier to adsorb intermediate in OER [8, 32]. The high angle annular dark field scanning transmission electron microscopy (HAADF-STEM) image and the corresponding elemental mapping results (Fig. 1c) display the Mn and O elements are uniformly distributed in the electrocatalyst with the relatively fewer Ru elements, demonstrating that Ru species are highly dispersed on Mn_3O_4. Therefore, Mn_3O_4 is the dominant body of the electrocatalyst composition, which supports Ru-RuO_2 nano-heterostructures to promote OER in acidic media. The SEM image in Fig. S1 (Supplementary data) shows that the bulky particles are unevenly anchored on carbon paper. All samples are connected tightly without obvious cracks, especially Ru-RuO_2/Mn_3O_4/CP shows a smooth surface. In order to avoid the interference of the strong characteristic peaks of the carbon paper that disturbs the phase of the catalyst composition (Fig. S2, Supplementary data), electrocatalyst powders obtained under the same experimental conditions with the absence of carbon paper are conducted for X-ray diffraction (XRD) measurement. As depicted in Fig. 1d, the XRD pattern displays the crystallographic information of Mn_3O_4, RuO_2, and Ru. The $MnCl_2$ precursor was oxidized to the tetragonal Mn_3O_4 (PDF # 24-0734) after 6 h calcination at 400 °C. Alternatively, the corresponding XRD pattern presents the tetragonal RuO_2 (PDF # 88-0286) and hexagonal Ru (PDF # 06-0663) in the absence of manganese precursor, which suggests the incomplete oxidation of $RuCl_3$. As a result, the Ru-RuO_2/Mn_3O_4 contains characteristic peaks of three phases, which were synthesized by introducing ruthenium and manganese precursors together into the impregnation solution approach. Besides, the FWHM of (110), (101), and (211) crystal facets for RuO_2 in Ru-RuO_2/Mn_3O_4 are larger than those in Ru-RuO_2, indicating a smaller particle size of RuO_2 in Ru-RuO_2/Mn_3O_4 according to the Debye-Scherrer's equation. This is expected to expose more active sites, that are beneficial to catalytic activity [33]. To determine the mass loading of Ru and Mn on the carbon paper, results from inductively coupled plasma mass spectrometry (ICP-MS) show that the content ratio of Ru to Mn is about 1:6 in Ru-RuO_2/Mn_3O_4/CP (Table S1, Supplementary data). In addition, the structural characterization of Ru-RuO_2/CP (Fig. S3, Supplementary data) also shows Ru (100) andRuO_2 (110) heterostructures, and the corresponding selected area electron diffraction (SAED) pattern (inset of Fig. S3) further demonstrates the polycrystalline nature with distinct diffraction rings belonging to Ru and RuO_2. Interestingly, the TEM image of Mn_3O_4/CP (Fig. S4, Supplementary data) exhibits the parallel and regular lattice fringes of Mn_3O_4 (200) with corresponding fast Fourier transform (FFT) pattern, which indicates that the applied calcination temperature and holding time are favorable for crystallization of Mn_3O_4 rather than forming other manganese oxides of polymorphs.

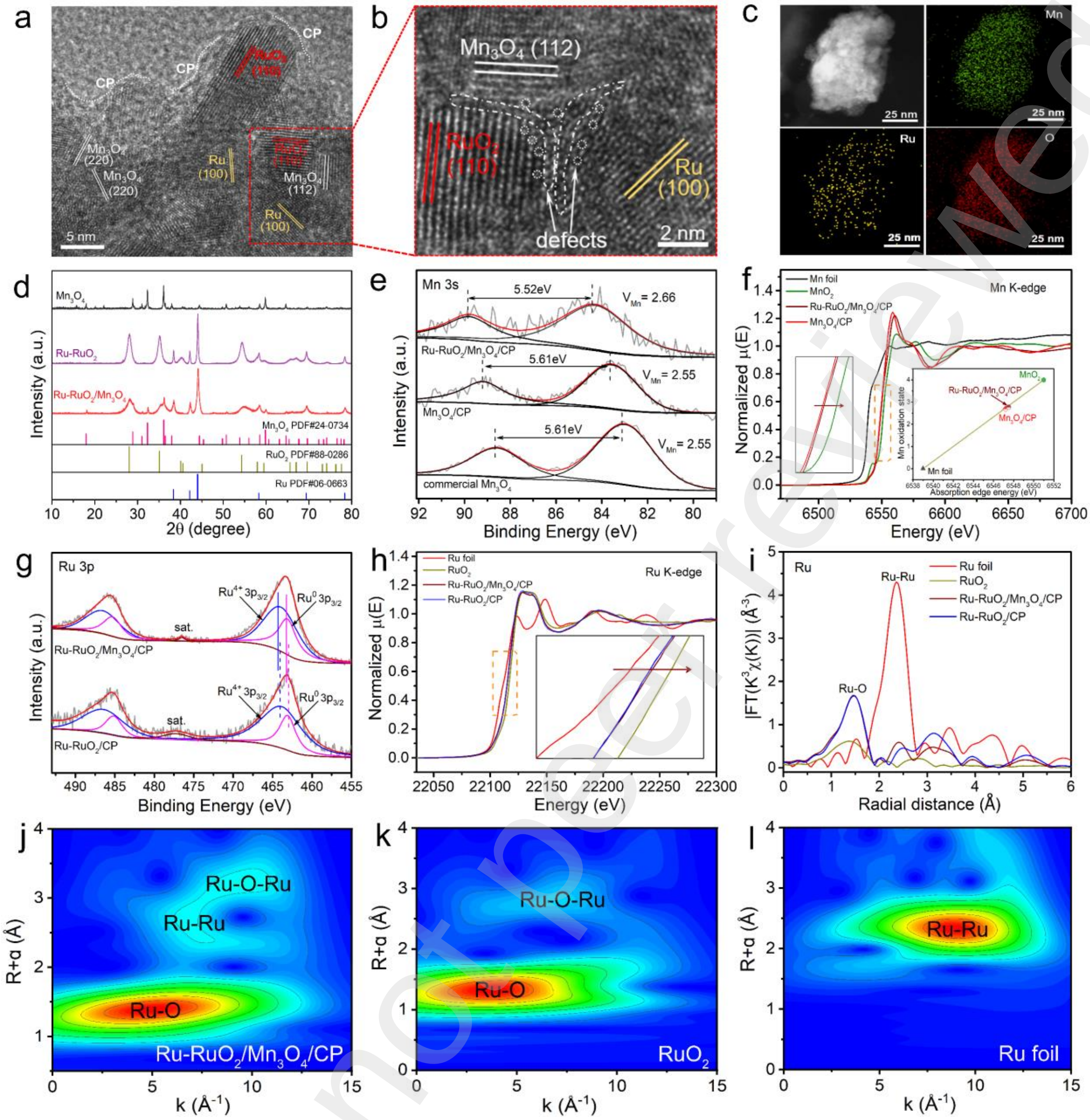

Fig. 1. Structural characterization of Ru-RuO_2/Mn_3O_4/CP. (a) TEM image; **(b)** HRTEM image for the zone indicated by a red dotted box from Fig. 1a; **(c)** HAADF-STEM image and elemental mappings of Mn, Ru, and O; **(d)** Powder X-ray diffraction patterns; **(e)** Mn 3s XPS spectrum; **(f)** Normalized XANES spectra of Mn foil, MnO_2, Ru-RuO_2/Mn_3O_4/CP, and Mn_3O_4/CP, the bottom right inset: the relationship of Mn oxidation state vs. adsorption edge energy for above samples at the Mn K-edge; **(g)** Ru 3p XPS spectrum; **(h)** Normalized XANES and **(i)** EXAFS spectra of Ru foil, RuO_2, Ru-RuO_2/Mn_3O_4/CP, and Ru-RuO_2/CP at the Ru K-edge. Wavelet transforms for the k^2-weighted Ru K-edge EXAFS signals of **(j)** Ru-RuO_2/Mn_3O_4/CP, **(k)** RuO_2, and **(l)** Ru foil.

X-ray photoelectron spectroscopy (XPS) measurements are qualified for investigating the electronic structure of the fresh electrocatalysts (Ru-RuO_2/Mn_3O_4/CP, Ru-RuO_2/CP, and Mn_3O_4/CP) before acidic OER. The Mn $2p_{3/2}$ spectra in Fig. S5 and Table S2 (Supplementary data) show that three deconvoluted curves at 641.00, 642.10, and 644.40 eV correspond to Mn^{2+}, Mn^{3+}, and Mn^{4+} oxidation states of Ru-RuO_2/Mn_3O_4/CP, respectively [34, 35]. Compared with Mn_3O_4/CP and commercial Mn_3O_4, the binding energy of manganese's valence state in Ru-RuO_2/Mn_3O_4/CP has shifted to the positive direction, which is attributed to the influence of the load of Ru-RuO_2 nano-heterostructures. According to the literature, the Mn 3s exchange splitting ΔE_{3s} is used to determine Mn valences (V_{Mn}) by the linear equation: $V_{Mn} = 9.67–1.27\Delta E_{3s}$ [36, 37]. As shown in Fig. 1e, the average valence states of Mn in the Ru-RuO_2/Mn_3O_4/CP and Mn_3O_4/CP are 2.66 (ΔE_{3s}=5.52 eV) and 2.55 (ΔE_{3s}=5.61 eV) respectively, which are close to the average valence in commercial Mn_3O_4. To further assess the Mn valences in Ru-RuO_2/Mn_3O_4/CP, the normalized spectra of X-ray absorption near-edge structure (XANES) spectra at the Mn K-edge of samples are analyzed. Fig. 1f shows the absorption edge of Ru-RuO_2/Mn_3O_4/CP and Mn_3O_4/CP is located between Mn foil and commercial MnO_2, suggesting its valence between 0 and +4. But the absorption edge of Ru-RuO_2/Mn_3O_4/CP shifts to the higher energy (left inset of Fig. 1f), which means that the Mn atoms in the Ru-RuO_2/Mn_3O_4/CP have the higher valence state than those in Mn_3O_4/CP. Based on the calculated valence states in the bottom right inset of Fig. 1f, the average valence of Mn atoms in the Ru-RuO_2/Mn_3O_4/CP and Mn_3O_4/CP are approximately +2.77 and +2.69, which is closely consistent with the XPS results [20]. The sequential valence gradient (Mn^{2+}/ Mn^{3+}/ Mn^{4+}) and a wide range of Mn-O bond length in Mn_3O_4 substrate are expected to operate as an effective sacrificial component, reducing the driving force for Ru-RuO_2 nano-heterostructures dissolution [34]. The extended X-ray absorption fine structure (EXAFS) with Fourier transform is performed to study the radial distribution function (RDF) of Mn atoms in Fig. S6, the fresh Ru-RuO_2/Mn_3O_4/CP shows stronger intensity corresponding to the Mn-O bond first coordination shell in comparison to Mn_3O_4/CP. However, the secondary coordination peak can be designated as the Mn-O-Mn bond of Ru-RuO_2/Mn_3O_4/CP, which is weaker and shorter than that of Mn_3O_4/CP, suggesting the distorted coordination environment around the Mn center due to the interactive coupling with Ru-RuO_2 heterostructures.

Further XPS analyses for both Ru-RuO_2/Mn_3O_4/CP and Ru-RuO_2/CP are applied to deeply understand the interaction of electrons between Ru and RuO_2. Consequently, the Ru 3p XPS spectra is given in Fig. 1g. Four peaks are deconvoluted in the high-resolution Ru 3p XPS spectrum for Ru-RuO_2/Mn_3O_4/CP, where the two peaks at 463.91 and 486.47 eV are respectively indexed to Ru $3p_{3/2}$ and Ru $3p_{1/2}$ of Ru (IV), and those at 463.11 and 485.27 eV could be assigned to Ru $3p_{3/2}$ and Ru $3p_{1/2}$ of Ru (0) [17, 38]. It is observed that the Ru 3p spectra for Ru-RuO_2/Mn_3O_4/CP slightly shifts to the higher binding energies relative to the Ru 3p of Ru-RuO_2/CP, giving the differences of 0.09 eV and 0.03 eV for Ru (IV) $3p_{3/2}$ and Ru (0) $3p_{3/2}$, respectively (Table S3, Supplementary data). This implies the Ru (IV) species in Ru-RuO_2/Mn_3O_4/CP is somewhat electron-scarcer than Ru-RuO_2/CP, probably as a result of the presence of the Mn_3O_4 substrate that may lead to effective interfacial charge transfer. According to previous studies [19, 39], the Ru species with a higher oxidation state in the Ru-based electrocatalysts could enhance the OER activity. The high-resolution O 1s spectra of Ru-RuO_2/Mn_3O_4/CP (Fig. S7, Supplementary data) exhibits four deconvoluted peaks at 529.8 eV, 530.3 eV, 531.9 eV, and 533.1 eV, which belong to Ru-O, Mn-O, surface adsorption oxygen (O_{ads}), and adsorbed water (H_2O_{ads}) [38, 40, 41]. Fig. 1h presents the normalized Ru K-edge XANES spectra, in which the RuO_2, Ru-RuO_2/Mn_3O_4/CP, and Ru-RuO_2/CP all display similar absorption edge and post-edge oscillations. In addition, the peak intensities of corresponding white-lines are sharply higher than that of reference Ru foil, which suggests rather higher chemical states of the Ru atoms in those three samples. It is observed that the absorption edges of Ru-RuO_2/Mn_3O_4/CP and Ru-RuO_2/CP locate between the reference Ru foil and commercial RuO_2. This indicates that the averaged Ru valence falls in the value of 0~4, which can be ascribed to the formation of Ru-RuO_2 nano-heterostructures. However, compared to Ru-RuO_2/CP, a positive shift in the absorption edge can be observed for the Ru-RuO_2/Mn_3O_4/CP (inset of Fig. 1h), demonstrating that the introduction of Mn_3O_4 substrate results in the valent increase of Ru. The results of Ru K-edge XANES are also in accordance with the Ru 3p XPS results. The corresponding extended X-ray absorption fine-structure (EXAFS) spectrum of Ru-RuO_2/Mn_3O_4/CP and Ru-RuO_2/CP at the Ru K-edge show a dominant peak at around 1.47 Å (Fig. 1i), in accordance with the first coordination shell of Ru-O scattering path, which is larger than RuO_2 (≈1.38 Å). This signifies that the formation of Ru-RuO_2 nano-heterostructures is followed by a modest variation in the length of the Ru-O bond. In addition, the peak intensity of Ru-Ru bond first scattering interaction located at around 2.41 Å and 2.46 Å in the Ru-RuO_2/Mn_3O_4/CP and Ru-RuO_2/CP are lower than that of Ru-O bond, which means the number of Ru-Ru bond is fewer than Ru-O bond.

Wavelet transformations (WT) were used to further investigate the Ru-O and Ru-Ru coordination environment in Ru-RuO_2/Mn_3O_4/CP. The WT maximum for the pronounced Ru-O scattering path (~ 5.0 $Å^{-1}$, Fig. 1j) in Ru-RuO_2/Mn_3O_4/CP is larger than that in the RuO_2 (~ 4.1 $Å^{-1}$, Fig. 1k), indicating that the Ru element in Ru-O scattering interaction is partially replaced by the heavier element of Ru/Mn to form a portion of Ru-Ru/Ru-Mn scattering interaction [42-44]. Similarly, one sub-center located at ~ 9.6 $Å^{-1}$ is ascribed to the Ru-O-Ru coordination for Ru-RuO_2/Mn_3O_4/CP, which is larger than that in the RuO_2 (~ 7.5 $Å^{-1}$). Furthermore, the other sub-center situated at ~ 7.2 $Å^{-1}$ is assignable to the Ru-Ru coordination for Ru-RuO_2/Mn_3O_4/CP, whose intensity is weaker than that of Ru foil (~ 8.9 $Å^{-1}$, Fig. 1l). Since Ru-RuO_2 nano-heterostructures are loaded on the Mn_3O_4 substrate, the Ru-Ru scattering interaction is partially substituted by the lighter element of Mn, resulting in the shorter sub-center. In a nutshell, XPS and XAFS characterization results provide clear evidence of the formation of the Ru-RuO_2 nano-heterostructures combined with the multivalent Mn_3O_4 substrate.

3.2 Acidic OER performance

The OER performance of these prepared electrocatalysts in O_2-saturated 0.5 M H_2SO_4 was investigated by using a standard three-electrode configuration. For comparison's sake, commercial RuO_2 and Ru/C electrocatalysts were also investigated under the same conditions. Typically, the electrocatalytic activity was measured by the linear sweep voltammetry (LSV) method (Fig. 2a). It can be clearly observed that Ru-RuO_2/Mn_3O_4/CP exhibits the lowest overpotential at 10 mA cm^{-2} (η_{10} = 182 mV) than that of Ru-RuO_2/CP (η_{10} = 217 mV), Mn_3O_4/CP (η_{10} = 289 mV), and commercial RuO_2 (η_{10} = 295 mV). Interestingly, the commercial Ru/C exhibits a gradually increased anodic current response at the beginning of the LSV scan, which also shows a similar onset potential to Ru-RuO_2/Mn_3O_4/CP in appearance, but it should be attributed to the phenomenon that the metallic Ru itself is easily oxidized [45]. The corresponding Tafel analysis exhibits that the Ru-RuO_2/Mn_3O_4/CP reaches the smallest slope of 97.4 mV dec^{-1} (Fig. S8, Supplementary data) compared with the Ru-RuO_2/CP (164.5 mV dec^{-1}), commercial RuO_2 (141.7 mV dec^{-1}), and Mn_3O_4/CP (372.9 mV dec^{-1}), suggesting the fastest OER kinetics and electron transfer occur on the defect-rich surface of Ru-RuO_2/Mn_3O_4/CP among various electrocatalysts. Particularly, the result in Fig. 2b shows that Ru-RuO_2/Mn_3O_4/CP could reach a remarkable mass activity of 1324.6 A g_{Ru}^{-1} (normalized by Ru) at 1.50 V vs. RHE, which is roughly 110.4 times and 10.7 times higher than those of commercial RuO_2 (12 A g_{Ru}^{-1}) and commercial Ru/C (123.3 A g_{Ru}^{-1}). Most importantly, compared with commercial electrocatalysts, such an excellent OER performance of Ru-RuO_2/Mn_3O_4/CP can be obtained directly on carbon paper with a loading mass of only 42.2 μg Ru precious metal.

The electrochemical impedance spectroscopy (EIS) from 100 kHz to 0.01 kHz for all electrocatalysts is performed to further explore the difference of catalytic kinetics. In general,

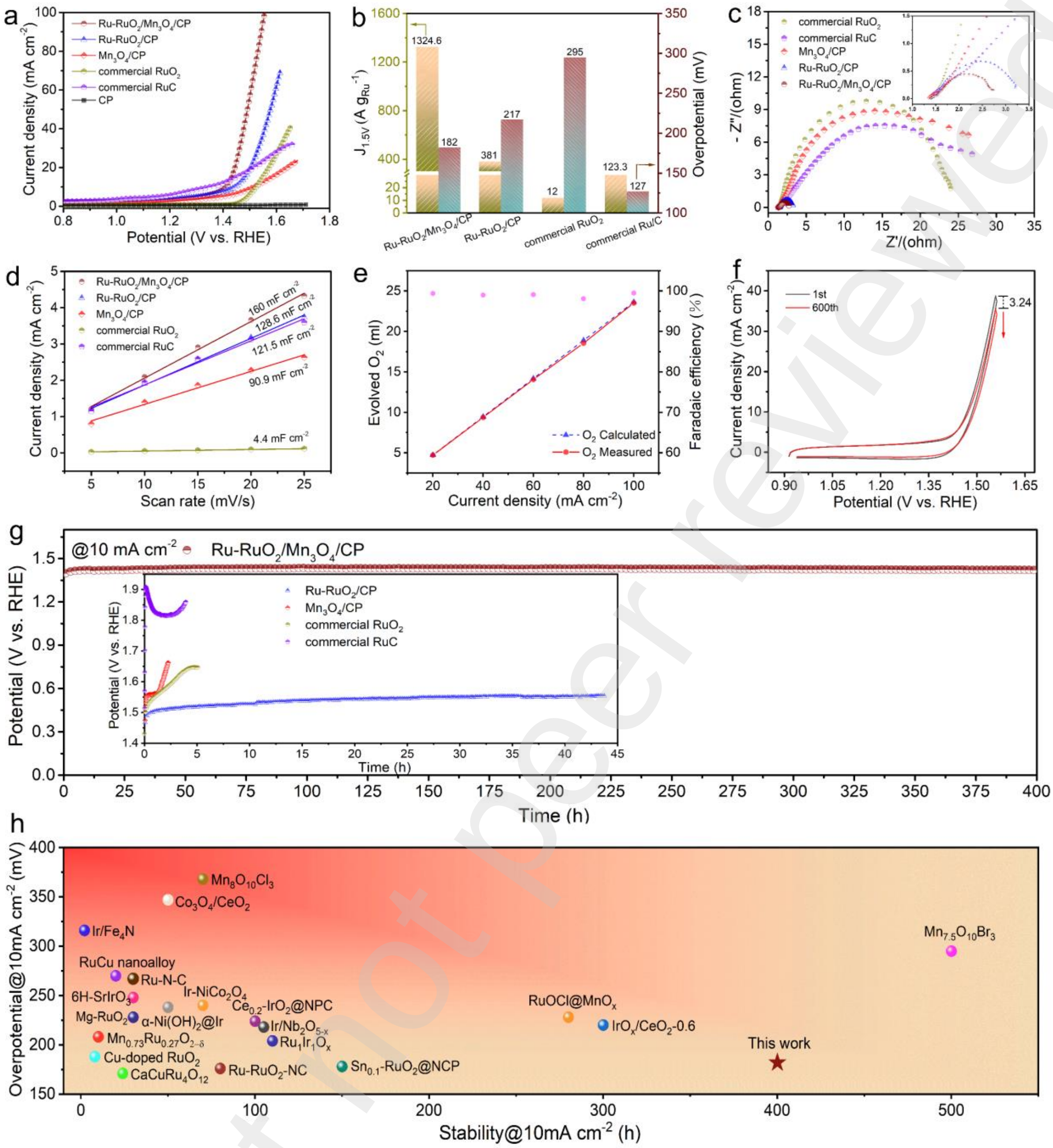

Fig. 2. Electrocatalytic OER performance. (a) LSV curves with iR-correction of various electrocatalysts in 0.5 M H_2SO_4; **(b)** Overpotentials at 10 mA cm^{-2} and normalized mass activities at 1.50 V vs. RHE of Ru-RuO_2/Mn_3O_4/CP, Ru-RuO_2/CP, commercial RuO_2, and commercial Ru/C; **(c)** Nyquist plots at 1.50 V vs. RHE of various catalysts; **(d)** C_{dl} of various catalysts; **(e)** The FE of Ru-RuO_2/Mn_3O_4/CP. **(f)** CV cycles of Ru-RuO_2/Mn_3O_4/CP; **(g)** Chronopotentiometry curves at 10 mA cm^{-2} for Ru-RuO_2/Mn_3O_4/CP and the other electrocatalysts inset; **(h)** Comparison of OER activity for various reported electrocatalysts (Table S5, Supplementary data), the x and y axes represent the stability and overpotential at 10 mA cm^{-2}.

three components including double-layer capacitance, charge-transfer resistance, and solution resistance exist in Nyquist plots (Fig. S9, Supplementary data). As shown in Fig. 2c, there are two semicircle curves, where the high frequency resistance can be employed to determine the charge transfer resistance (R_{ct}) relevant to electrocatalytic kinetics, and the low frequency resistance can be used to efficiently measure transmit electronic signals at the interfaces between electrodes and electrolytes [46]. At the potential of 1.50 V vs. RHE, all the samples exhibit similar large semicircles, corresponding to the dramatic OER process [47]. Consequently, the results present that the semicircles for both Ru-RuO_2/Mn_3O_4/CP and Ru-RuO_2/CP are much smaller than those for other samples mentioned above, implying that the built-in Ru-RuO_2 nano-heterostructures contribute to the formation of electronic transport channels at Ru|RuO_2 interfaces and it thus effectively accelerate the OER kinetics [23, 48, 49]. Notably, the Ru-RuO_2/Mn_3O_4/CP possesses the minimum R_{ct} of only 1.26 Ω among all samples, indicating that the introduction of Mn_3O_4 substrate can further promote electron transfer at the interface so as to achieve its fastest OER dynamics. Additionally, cyclic voltammetry experiments were carried out at various scan speeds in the non-Faraday region to acquire C_{dl} for estimation of the relative electrochemically active surface area (Fig. S10, Supplementary data) [50]. Fig. 2d shows that the C_{dl} value of Ru-RuO_2/Mn_3O_4/CP (160 mF cm^{-2}) are higher than Ru-RuO_2/CP (128.6 mF cm^{-2}), commercial Ru/C (121.5 mF cm^{-2}), Mn_3O_4/CP (90.9 mF cm^{-2}), and commercial RuO_2 (4.4 mF cm^{-2}), suggesting that the Ru-RuO_2 nano-heterostructures loaded on Mn_3O_4 substrate possess more active sites and thus boost acidic OER performance. The water displacement method was implemented to calculate the Faradaic efficiency (FE) of OER (Fig. S11, Supplementary data) [41]. The outcome in Fig. 2e demonstrates that under various current densities, the measured oxygen volume approaches 100% FE and agrees well with the theoretical values calculated by Faraday's law of electrolysis.

The durability of the $Ru-RuO_2/Mn_3O_4/CP$ under harsh acidic conditions is another critical criterion for practical applications. Compared with the $Ru-RuO_2/CP$ and commercial RuO_2 (Fig. S12, Supplementary data), the $Ru-RuO_2/Mn_3O_4/CP$ shows a slight degradation of 3.24 mA cm^{-2} after 600 cyclic voltammogram cycles (CV) in the range from 0.91 V to 1.56 V vs. RHE (Fig. 2f). Additionally, these as-prepared OER electrocatalysts are investigated by chronopotentiometry (CP) test at 10 mA cm^{-2}, which is recommended as a widely adapted benchmark OER stability testing condition [51, 52]. As depicted in Fig. 2g, it is noteworthy that $Ru-RuO_2/Mn_3O_4/CP$ remains a quite steady performance for the 400 h CP test, implying its outstanding long-term stability for acidic OER. By contrast, commercial RuO_2, commercial Ru/C, and as-synthesized Mn_3O_4/CP exhibit rapid activity decays during the OER stability test. Although the as-synthesized $Ru-RuO_2/CP$ shows a relatively slow decay at 10 mA cm^{-2} for more than 40 h in the inset of Fig. 2g, the stability in $Ru-RuO_2/CP$ decreases faster with the increase of current density (Fig. S13-15, Supplementary data). The superior OER stability of $Ru-RuO_2/Mn_3O_4/CP$ clearly emphasizes the critical role of Mn_3O_4 substrate. To summarize, Fig. 2h and Table S5 (Supplementary data) show a comparison of the performance of $Ru-RuO_2/Mn_3O_4/CP$ with previously reported acidic OER electrocatalysts in activity and stability, evidently indicating that $Ru-RuO_2/Mn_3O_4/CP$ exhibits considerable OER performance in the 0.5 M H_2SO_4 electrolyte comparatively, outperforming other recently reported noble metal-based electrocatalysts.

3.3 Exposition of the sacrificing oxidation strategy of Mn_3O_4 substrate

To shed light on the protective mechanism of Mn_3O_4 substrate against $Ru-RuO_2$ nano-heterostructures, we investigated the electronic structural change of $Ru-RuO_2/Mn_3O_4/CP$ and $Ru-RuO_2/CP$ before and after the acidic OER process. It is known that the process of longstanding current input and continuous adsorption and desorption of intermediates (H_2O, OH^*, O^*, and OOH^*) is the ordeal for electrocatalysts lifetime, which is also accompanied with excessive oxidation and dissolution of metal active center ions ($Ru^{\delta>4+}$). Hence, determining the oxidation degree of Ru ions before and after the stability test is necessary to evaluate their antioxidant ability. As exhibited in the XPS spectrum of Fig. 3a, the Ru $3p_{3/2}$ in Ru-RuO_2/CP after 24 h chronopotentiometry test at 10 mA cm^{-2} presents a higher oxidation state than that in the fresh Ru-RuO_2/CP, which displays the positive shifts of 0.36 and 0.07 eV toward the high binding energy for Ru (IV) $3p_{3/2}$ and Ru (0) $3p_{3/2}$, respectively. The decrease of Ru (0) $3p_{3/2}$ proportion implies that some Ru^{4+} species in the heterostructures is over-oxidized and dissolved into the electrolyte, at the same time, the adjacent metallic Ru is partially oxidized to Ru^{4+} as a supplement source. In comparison, the Ru-RuO_2/Mn_3O_4/CP shows the positive shifts of only 0.11 and 0.03 eV for Ru (IV) $3p_{3/2}$ and Ru (0) $3p_{3/2}$ after 24 h stability test (Fig. 3b), evidencing that the introduction of Mn_3O_4 substrate can suppress the over-oxidation of the Ru species, which contributes to the highly improved antioxidant ability and stability of Ru-RuO_2 nano-heterostructures. It can be found in Fig. 3c-d that the Mn^{2+}, Mn^{3+}, and Mn^{4+} in Ru-RuO_2/Mn_3O_4/CP exhibit varied degrees of positive energy shift and the average valence of Mn species in Mn 3s spectra increases to 3.05 from 2.66 after stability test. In addition, the TEM image (Fig. S16 a, Supplementary data) further confirms that the highly dispersed Ru-RuO_2 nano-heterostructures primary grains are anchored in the Mn_3O_4 substrate without reconstruction or aggregation after 150 hours' stability test, and the corresponding elemental mapping also confirms that Ru, Mn, and O atoms still exist in Ru-RuO_2/Mn_3O_4/CP, but there are fewer Ru and Mn atoms than the pristine state for all cases of comparison electrocatalysts, denoting that the metal ions of Ru-RuO_2/Mn_3O_4/CP more tardily dissolve in electrolyte during a long stability test. This result demonstrates that the excellent stability of Ru-RuO_2/Mn_3O_4/CP is benefited from the synergistic effect between Mn_3O_4 substrate and Ru-RuO_2 nano-heterostructures. Comparatively, Mn_3O_4 is more susceptible to oxidation than Ru and RuO_2 under large overpotential in the OER range, which consequently protects Ru species from over-oxidation and guarantees the stable existence of active sites in Ru-

RuO_2/Mn_3O_4/CP.

Time-dependent Ru ions dissolution results in Fig. 3e can further reflect the importance of Mn_3O_4 substrate. In order to monitor the dissolution of the noble metal, we measured Ru ion dissolution in the electrolyte during 24 h CP test at 10 mA cm^{-2} via ICP-MS (Table S6, Supplementary data). The histogram discloses that the dissolution amount of Ru ion in Ru-RuO_2/CP is larger than that in Ru-RuO_2/Mn_3O_4/CP during the same time, suggesting that Ru ions are leached out of the Ru-RuO_2/CP rapidly during the stability test. Besides, the Ru dissolution rate of Ru-RuO_2/CP in the absence of Mn_3O_4 substrate becomes faster with the increase of testing time. When the test is conducted for 24 h, the dissolution ratio of Ru element in Ru-RuO_2/Mn_3O_4/CP is only 89.73 ppb, which is approximately half of the dissolution ratio in Ru-RuO_2/CP. Full range spectrum results of XPS further confirm the remained Ru in the two samples after the stability test (Fig. S17, Supplementary data). The dramatically weakened peak intensities of Ru 3p and 3d in Ru-RuO_2/CP indicate a large amount of Ru ion dissolution, which is in accordance with the results of ICP-MS. In contrast to Ru-RuO_2/CP, the Ru 3p and 3d peak intensities do not decrease distinctly in Ru-RuO_2/Mn_3O_4/CP. Alternatively, the peak intensity of Mn 2p is weakened significantly, implying that cost-effective Mn atoms are sacrificed to protect noble Ru atoms. Therefore, we conjecture that the sacrificing oxidation of the Mn_3O_4 substrate is capable of stabilizing the entire electrocatalyst by decreasing the driving force of dissolution of Ru-RuO_2.

Moreover, the important role of Mn_3O_4 substrate is also indicated by the ex-situ XANES spectra for the Ru-RuO_2/CP and Ru-RuO_2/Mn_3O_4/CP electrocatalysts before and after OER. Fig. 3f demonstrates that the OER process increases the valence state of Mn species in Ru-RuO_2/Mn_3O_4/CP while only slightly increasing the valence state of Ru species (Fig. S18 a, Supplementary data). The slight positive shift of the Ru K-edge indicates the positive accumulation of Ru^{4+} species (i.e. RuO_2) in Ru-RuO_2/Mn_3O_4/CP, which is beneficial to the electrocatalytic activity and stability in harsh acidic environment [53]. However, the Ru

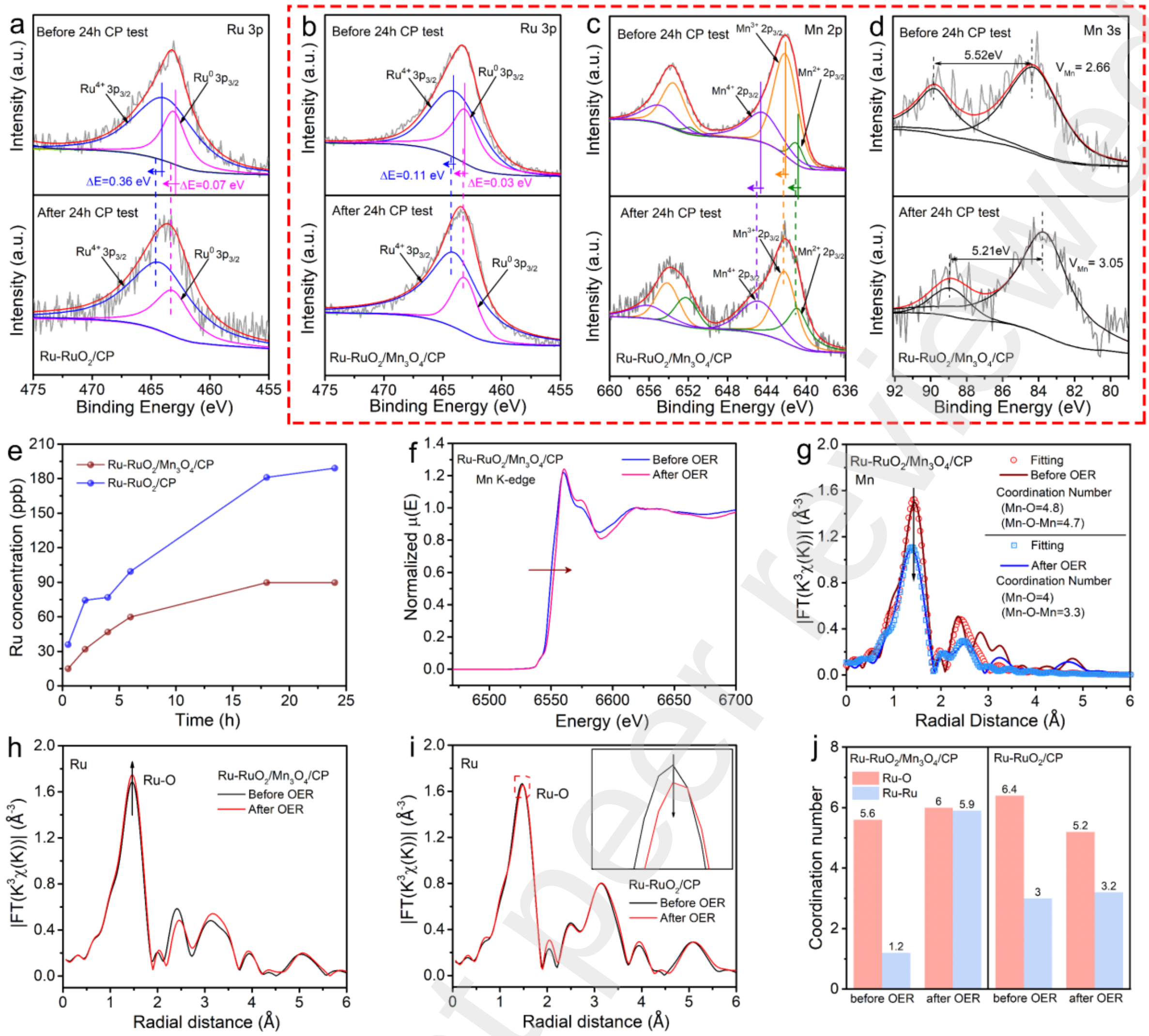

Fig. 3. Electronic and Atomic Structure Changes before and after OER. High-resolution XPS spectra of **(a)** Ru 3p$_{3/2}$ for Ru-RuO$_2$/CP before and after 24 h CP test at 10 mA cm^{-2}; High-resolution XPS spectra of **(b)** Ru 3p$_{3/2}$ **(c)** Mn 2p and **(d)** Mn 3s for Ru-RuO$_2$/Mn$_3$O$_4$/CP before and after 24 h CP test at 10 mA cm^{-2}; **(e)** Concentration of dissolved Ru ions in electrolyte during 24 h CP test; **(f)** Normalized XANES spectra at the Mn K-edge for Ru-RuO$_2$/Mn$_3$O$_4$/CP before and after the OER test; **(g)** The R-space curve-fitting curves in the Mn K-edge for Ru-RuO$_2$/Mn$_3$O$_4$/CP before and after OER; R-space of the EXAFS spectra at the Ru K-edge for **(h)** Ru-RuO$_2$/Mn$_3$O$_4$/CP and **(i)** Ru-RuO$_2$/CP before and after the OER test; **(j)** The coordination number of Ru-O and Ru-Ru for Ru-RuO$_2$/Mn$_3$O$_4$/CP and Ru-RuO$_2$/CP before and after the OER test.

K-edge in Ru-RuO$_2$/CP without the protection of Mn$_3$O$_4$ substrate shows an opposite shift after OER (Fig. S18 b, Supplementary data), namely, the decrease of valence state for Ru, implying that the dissolution rate of Ru ions is more predominant than the oxidation rate from metallic Ru to RuO_2. Furthermore, the coordination number (CN) obtained from EXAFS spectra exhibits the details of structural evolution (Table S7, Supplementary data). The R-space fitting curves in the Mn K-edge show that the CN of Mn-O decreases from 4.8 to 4, and the CN of Mn-O-Mn decreases from 4.7 to 3.3, suggesting the dissolution of Mn atoms after OER (Fig. 3g and Fig. S19, Supplementary data). The sacrificial dissolution of the Mn_3O_4 substrate is further revealed by the negative shift of next nearest-neighbor (Mn-O-Mn) in Ru-RuO_2/Mn_3O_4/CP, which is supported by the WT results (Fig. S20, Supplementary data). Specifically, since the electronegativity of Mn (1.55) is lower than that of Ru (2.20), Ru atom has a tendency to acquire electrons from Mn via O bridge, and thus the Mn_3O_4 substrate can effectively alleviate the over-oxidation of Ru atoms to turn into soluble $Ru^{\delta>4+}$ species during OER [32, 54]. The CNs' variation of Ru-O and Ru-Ru bonds are also investigated for the Ru-RuO_2/Mn_3O_4/CP and Ru-RuO_2/CP before and after acidic OER, and the results are given in Fig. 3h-j and Fig. S21-22 (Supplementary data). On one hand, the CN of Ru-O in Ru-RuO_2/Mn_3O_4/CP increases from 5.6 to 6, while such CN in Ru-RuO_2/CP decreases from 6.4 to 5.2 after OER. This is attributed to the probably existed O bridge between Ru and Mn. That is, the formation of Mn-O-Ru bonds could be the rationale behind this. Though the dissolution of metal Mn occurs in Ru-RuO_2/Mn_3O_4/CP during the reaction, the O bridge chemically interacted with adjacent Ru would be helpful to maintain the active valence state of Ru species for acidic OER. On the other hand, the CN of Ru-Ru in Ru-RuO_2/Mn_3O_4/CP considerably increases from 1.2 to 5.9, while such CN in Ru-RuO_2/CP slightly increases from 3 to 3.2. As validated by the WT results (Fig. S23-24, Supplementary data), the sub-center Ru-Ru bond in Ru-RuO_2/CP changes insignificantly, whereas the area of the Ru-Ru bond in Ru-RuO_2/Mn_3O_4/CP clearly extend, indicating that the content of the Ru-Ru bond increases. It suggests that the Ru atoms on the Mn_3O_4 substrate would bond with each other after Mn ions dissolution, which can remit the dissolution of Ru atoms. These results reflect that the

Mn_3O_4 substrate can effectively suppress the over-oxidation of Ru species in Ru-RuO_2/Mn_3O_4/CP during the violent oxygen evolution, highlighting the vital effect of sacrificing oxidation of Mn_3O_4 substrate.

3.4 Identification of OER mechanism

To further investigate the putative catalytic mechanism on commercial RuO_2, Ru-RuO_2/CP, and Ru-RuO_2/Mn_3O_4/CP, the pH-dependence measurements of their OER activities were conducted in the pH range of 0.3-1 (**Fig. 4**a and Fig. S25 in Supplementary data). The commercial RuO_2 shows different OER performance in the electrolyte with different pH values, suggesting the participation of lattice oxygen in the acidic OER that is proceeded on RuO_2 surface [10]. In contrast to the commercial RuO_2, both Ru-RuO_2/CP and Ru-RuO_2/Mn_3O_4/CP exhibit negligible pH dependence. That is, their current densities are almost constant in different pH values under varied OER overpotentials. The results reveal that Ru-RuO_2/CP and Ru-RuO_2/Mn_3O_4/CP follow proton coupled electron transfer (PECT) process, which is consistent with the characteristics of the adsorbate evolution mechanism (AEM) [20, 55]. The generation of oxygen via AEM pathway in acid electrolyte requires four protons and electrons, which can be separated into four steps: 1) $H_2O \rightarrow OH^* + H^+ + e^-$; 2) $OH^* \rightarrow O^* + H^+ + e^-$; 3) $O^* + H_2O \rightarrow OOH^* + H^+ + e^-$; 4) $OOH^* \rightarrow O_2 + H^+ + e^-$.[56] According to the literature [41, 57], the formed OH^* intermediates are electrophiles that can be identified by interacting with nucleophiles like methanol. As demonstrated in Fig. S26 (Supplementary data), the Ru-RuO_2/CP and Ru-RuO_2/Mn_3O_4/CP present smaller onset potentials than commercial RuO_2, signifying that the faster methanol oxidation reaction (MOR) and stronger adsorption capability of the OH^* intermediate occur on the catalyst surface.

To experimentally track the AEM pathway, *operando* differential electrochemical mass spectrometry (DEMS) with isotope labeling was carried out (Fig. 4b). We labeled the catalyst surface with ^{18}O in 0.5 M H_2SO_4 using $H_2{}^{18}O$ as the supporting solution, and then we measured the evolved O_2 in a normal 0.5 M H_2SO_4 solution (see Methods in Supplementary data). The signals of $^{32}O_2$ and $^{34}O_2$ observed on commercial RuO_2 (Fig. 4c) indicate that the OER gaseous product is generated on RuO_2 through the AEM and LOM pathway, in

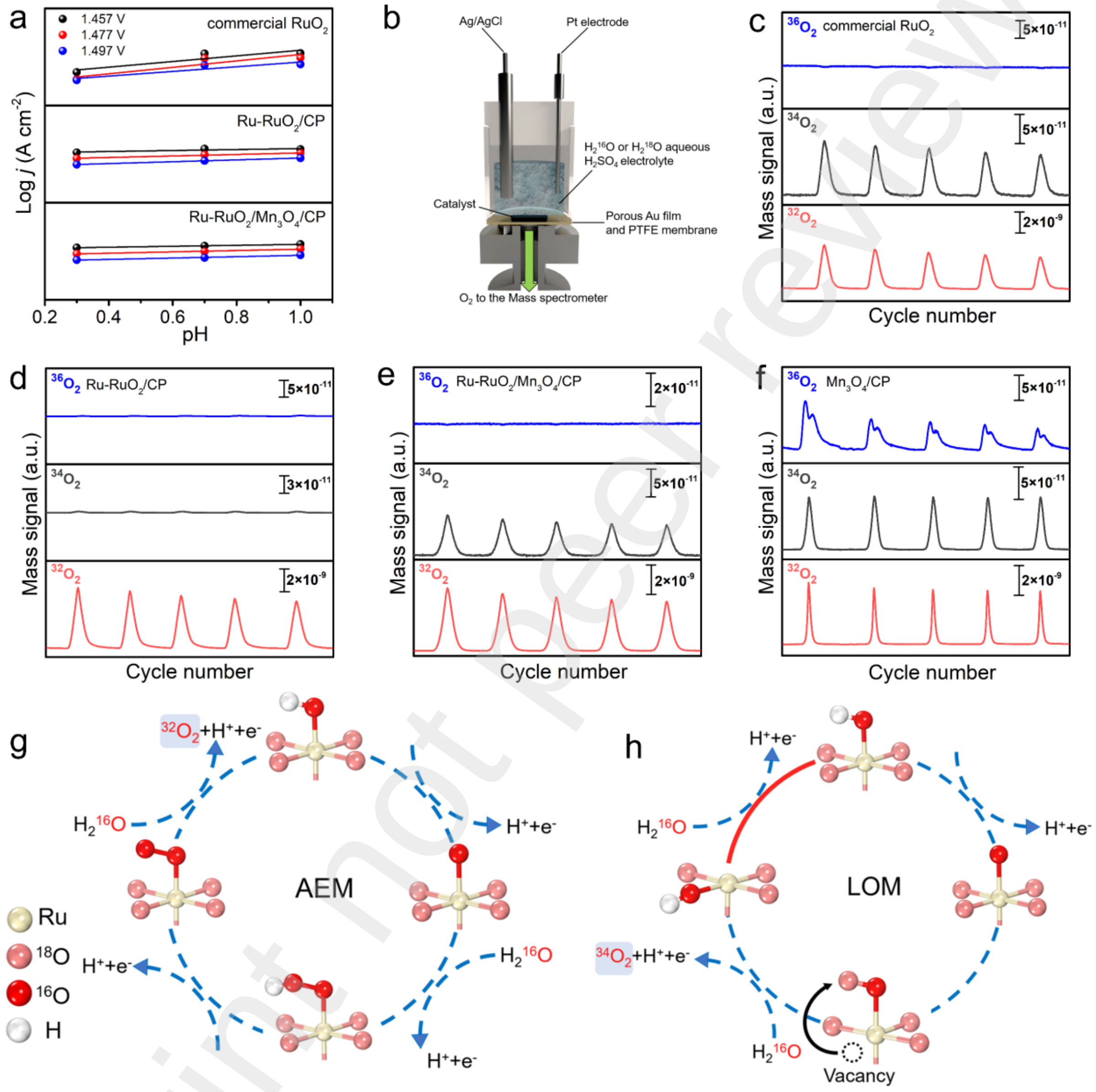

Fig. 4. OER mechanism analysis. (a) pH-independent OER activities for commercial RuO_2, Ru-RuO_2/CP, and Ru-RuO_2/Mn_3O_4/CP; **(b)** Schematic illustration of the operando DEMS; DEMS signals of $^{36}O_2$, $^{34}O_2$, and $^{32}O_2$ from the reaction products for ^{18}O-labeled **(c)** commercial RuO_2, **(d)** Ru-RuO_2/CP, **(e)** Ru-RuO_2/Mn_3O_4/CP and **(f)** Mn_3O_4/CP catalysts in $H_2{}^{16}O$ aqueous H_2SO_4 electrolyte; Schematic illustration of **(g)** AEM and **(h)** LOM pathway for OER on the RuO_2 (110) surface.

accordance with predecessors' research. However, no obvious $^{34}O_2$ signal can be observed on the Ru-RuO_2/CP (Fig. 4d), suggesting that the formation of heterostructures can effectively suppress the participation of lattice oxygen and change the reaction pathway from LOM to AEM [11, 58]. Furthermore, as shown in Fig. 4e, the Ru-RuO_2/Mn_3O_4/CP shows a similar variation trend compared with commercial RuO_2, and a small quantity of $^{34}O_2$ signal is probably derived from the Mn_3O_4 substrate. In short, the $^{32}O_2$ ($^{16}O^{16}O$) and $^{34}O_2$ ($^{16}O^{18}O$) signals reflect AEM and LOM pathways (Fig. 4g-h), respectively [11, 59]. The DEMS analysis, combined with the pH-dependence measurements, demonstrates that the OER proceeds via the AEM pathway on the Ru-RuO_2/CP and Ru-RuO_2/Mn_3O_4/CP, and the formation of Ru-RuO_2 heterostructures can effectively suppress the LOM pathway, leading to the boosted OER stability and activity under acidic condition.

The above experimental evidence shows that the Ru-RuO_2 heterostructures are the vital active centers of Ru-RuO_2/Mn_3O_4/CP. Furthermore, density functional theory (DFT) computations are conducted to analyze the partial density of states (PDOS) and the Gibbs free energies of Ru-RuO_2 heterostructure (Fig. S27a, Supplementary data) compared with RuO_2. The PDOS result demonstrates that the Ru 4d band center (ε_d(Ru)) versus the Fermi level is -4.348 eV in RuO_2, while such value is 4.163 eV in Ru-RuO_2 heterostructure, indicating that the d-band center is closer to the Fermi level after heterogenization. The upshifting of the d-band center after heterogenization strengthens the adsorption of oxygen intermediates [53, 60]. Besides, the corresponding calculated O 2p band centers (ε_p(O)) of RuO_2 and Ru-RuO_2 are -3.819 and -3.576 eV, respectively. With respect to the RuO_2 model, the Ru-RuO_2 model displays more anti-bonding states of O's 2p and Ru's 4d states, implying electrons transfer from the Mn to Ru atoms with O bridge modulation, which is consistent with the experimental findings above [20, 61]. These results indicate the covalency of Ru-O bond is increased after heterogenization, which is thermodynamically favorable to O-O coupling on Ru-RuO_2 heterostructures and kinetically in favor of adsorbate oxygen evolution [10, 16].

Based on the DEMS measurements, the Gibbs free energies of OER via AEM pathway are calculated on the optimized RuO_2 (110) and on the Ru^{4+} site on Ru-RuO_2 heterostructure. The result in Fig. S27b-29 (Supplementary data) shows that the formation of *OOH is the potential-determining step (PDS) for both RuO_2 and Ru-RuO_2. Such PDS requires an uphill energy gap of 1.711 eV on Ru-RuO_2 which is 0.659 eV less than that on RuO_2. As a result, the thermodynamic advantage of Ru-RuO_2 heterostructures over pure RuO_2 is therefore demonstrated.

3.5 Electrocatalysis practical application demonstration

Finally, in order to confirm the viability of Ru-RuO_2/Mn_3O_4/CP for larger-scale practical applications, a flow-type electrolysis system was assembled by using Ru-RuO_2/Mn_3O_4/CP, Ru-RuO_2/CP, and commercial RuO_2 as the anode as well as the commercial Pt/C (20 wt%) as the cathode and separated by a Nafion membrane (Fig. 5a and Fig. S30 in Supplementary data). The polarization curves (without iR correction) in Fig. 5b demonstrate an apparent improvement in cell performance while maintaining a constant cathode side preparation condition at ambient temperatures. Obviously, the cell performance of the Ru-RuO_2/Mn_3O_4/CP tested in the PEMWE is superior to that of the Ru-RuO_2/CP and commercial RuO_2. With its high catalytic activity, the Ru-RuO_2/Mn_3O_4/CP reaches a current density of 100 and 500 mA cm^{-2} at 1.787 and 2.111 V, respectively. However, to reach the same performances above, the Ru-RuO_2/CP needs higher potentials of 1.845 and 2.194 V, and the commercial RuO_2 has a slow dynamic growth trend that prevents it from growing faster than 100 mA cm^{-2} even at 2.5 V. Besides, upon applying a constant current of 50 mA cm^{-2} (Fig. 5c), the Ru-RuO_2/Mn_3O_4/CP electrolyzer can steadily work for more than 65 h. But the stability of the Ru-RuO_2/CP electrolyzer fluctuates greatly and commercial RuO_2 electrolyzer displays poor tolerance throughout the test. In consequence, the Ru-RuO_2/Mn_3O_4/CP electrolyzer possesses promising activity and stability of water electrolysis at ambient temperatures.

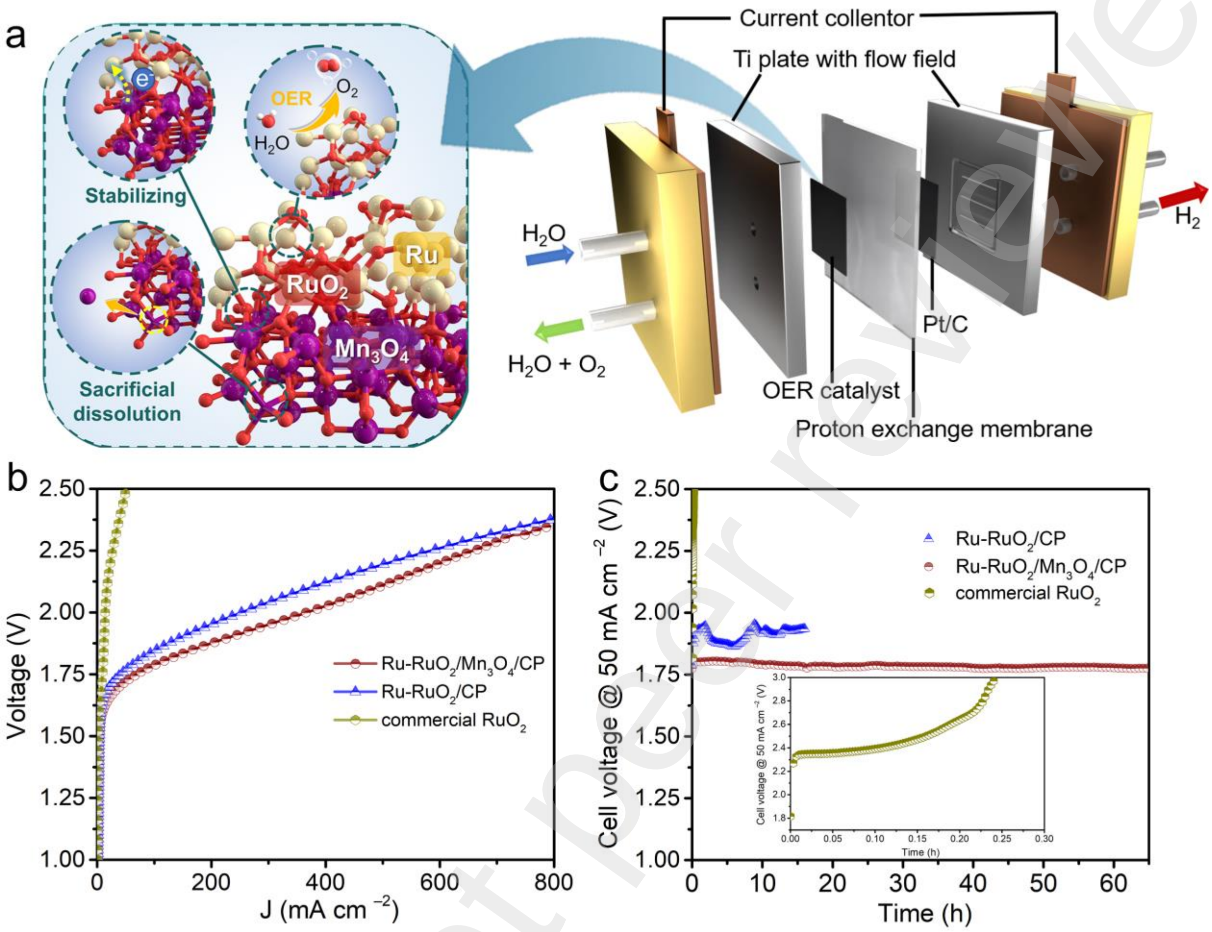

Fig. 5. PEM electrolyzer demonstration. (a) Schematic illustration of the sacrificing oxidation strategy of Mn_3O_4 substrate for Ru-RuO_2 nano-heterostructures and PEM electrolyzer device; **(b)** Polarization curves of a PEM electrolyzer measured at ambient temperatures; **(c)** Chronopotentiometry tests at 50 mA cm^{-2} in the PEM electrolyzer measured at ambient temperatures.

4.Conclusion

In summary, we demonstrate that the Ru-RuO_2/Mn_3O_4/CP catalyst exhibits significantly boosted activity with an overpotential of merely 182 mV at 10 mA cm^{-2}, accompanied with enhanced stability of 400 h for acidic OER. The improved catalytic stability is ascribed to the introduction of Mn_3O_4 substrate, which can protect active Ru^{4+} species in Ru-RuO_2 nano-heterostructures from over-oxidation, thus effectively alleviating the dissolution of Ru in acidic electrolytes via sacrificing the Mn_3O_4 substrate itself for preferential oxidation. Besides, the DEMS and DFT calculations results confirm that the formation of Ru-RuO_2 nano-heterostructures can effectively increase the d-band center of Ru and greatly suppress the LOM pathway, resulting in the enhanced OER activity Ru-RuO_2/Mn_3O_4/CP. This work provides not only a perspective on investigating the sacrificing oxidation strategy of Mn_3O_4 substrate for Ru-based electrocatalysts but also the scientific evidence for the modulation of the OER pathway in Ru-RuO_2 nano-heterostructures.

Acknowledgment

The authors acknowledge the financial support of Guangdong Basic and Applied Basic Research Foundation (No. 2023A1515010940), Shenzhen Natural Science Fund (the Stable Support Plan Program No. 20220809160022001), National Natural Science Foundation of China (No. 21805187, 21975163), and the Shenzhen Science and Technology Programs (No. ZDSYS20220527171401003, KQTD20190929173914967). The authors also thank Shiyanjia Lab (www.shiyanjia.com) for the XPS characterizations.

Conflicts of interest

The authors declare that they have no known competing financial interests or personal relationships that could have appeared to influence the work reported in this paper.

References

[1] S. Hu, S. Ge, H. Liu, X. Kang, Q. Yu, B. Liu, Low‐Dimensional Electrocatalysts for Acidic Oxygen Evolution: Intrinsic Activity, High Current Density Operation, and Long‐Term Stability, Adv. Funct. Mater. 32 (2022), 2201726, https://doi.org/10.1002/adfm.202201726..

[2] L. An, C. Wei, M. Lu, H. Liu, Y. Chen, G.G. Scherer, A.C. Fisher, P. Xi, Z.J. Xu, C.H.

Yan, Recent Development of Oxygen Evolution Electrocatalysts in Acidic Environment, Adv. Mater. 33 (2021), 2006328, https://doi.org/10.1002/adma.202006328.

[3] Z.Y. Wu, F.Y. Chen, B. Li, S.W. Yu, Y.Z. Finfrock, D.M. Meira, Q.Q. Yan, P. Zhu, M.X. Chen, T.W. Song, Z. Yin, H.W. Liang, S. Zhang, G. Wang, H. Wang, Non-iridium-based electrocatalyst for durable acidic oxygen evolution reaction in proton exchange membrane water electrolysis, Nat. Mater. 22 (2022) 100–108, https://doi.org/10.1038/s41563-022-01380-5.

[4] K. Sardar, E. Petrucco, C.I. Hiley, J.D. Sharman, P.P. Wells, A.E. Russell, R.J. Kashtiban, J. Sloan, R.I. Walton, Water-splitting electrocatalysis in acid conditions using ruthenate-iridate pyrochlores, Angew. Chem. Int. Ed. 53 (2014) 10960-10964, http://dx.doi.org/10.1002/anie.201406668.

[5] J. Song, C. Wei, Z.F. Huang, C. Liu, L. Zeng, X. Wang, Z.J. Xu, A review on fundamentals for designing oxygen evolution electrocatalysts, Chem Soc Rev. 49 (2020) 2196-2214, https://doi.org/10.1039/c9cs00607a..

[6] I.C. Man, H.Y. Su, F. Calle‐Vallejo, H.A. Hansen, J.I. Martínez, N.G. Inoglu, J. Kitchin, T.F. Jaramillo, J.K. Nørskov, J. Rossmeisl, Universality in Oxygen Evolution Electrocatalysis on Oxide Surfaces, ChemCatChem. 3 (2011) 1159-1165, http://dx.doi.org/10.1002/cctc.201000397.

[7] T. Reier, H.N. Nong, D. Teschner, R. Schlögl, P. Strasser, Electrocatalytic Oxygen Evolution Reaction in Acidic Environments - Reaction Mechanisms and Catalysts, Adv. Energy Mater. 7 (2017), 160127, https://doi.org/10.1002/aenm.201601275.

[8] Y. Lin, Y. Dong, X. Wang, L. Chen, Electrocatalysts for Oxygen Evolution Reaction in Acidic Media, Adv. Mater. 35 (2022), 221056, https://doi.org/10.1002/adma.202210565.

[9] Z.-F. Huang, J. Song, Y. Du, S. Xi, S. Dou, J.M.V. Nsanzimana, C. Wang, Z.J. Xu, X. Wang, Chemical and structural origin of lattice oxygen oxidation in Co–Zn oxyhydroxide oxygen evolution electrocatalysts, Nat. Energy. 4 (2019) 329-338,

https://doi.org/10.1038/s41560-019-0355-9.

[10] A. Grimaud, O. Diaz-Morales, B. Han, W.T. Hong, Y.L. Lee, L. Giordano, K.A. Stoerzinger, M.T.M. Koper, Y. Shao-Horn, Activating lattice oxygen redox reactions in metal oxides to catalyse oxygen evolution, Nat. Chem. 9 (2017) 457-465, https://doi.org/10.1038/nchem.2932.

[11] Y. Wen, P. Chen, L. Wang, S. Li, Z. Wang, J. Abed, X. Mao, Y. Min, C.T. Dinh, P. Luna, R. Huang, L. Zhang, L. Wang, L. Wang, R.J. Nielsen, H. Li, T. Zhuang, C. Ke, O. Voznyy, Y. Hu, Y. Li, W.A. Goddard, III, B. Zhang, H. Peng, E.H. Sargent, Stabilizing Highly Active Ru Sites by Suppressing Lattice Oxygen Participation in Acidic Water Oxidation, J. Am. Chem. Soc. 143 (2021) 6482-6490, https://doi.org/10.1021/jacs.1c00384.

[12] Y. Yao, S. Hu, W. Chen, Z.-Q. Huang, W. Wei, T. Yao, R. Liu, K. Zang, X. Wang, G. Wu, W. Yuan, T. Yuan, B. Zhu, W. Liu, Z. Li, D. He, Z. Xue, Y. Wang, X. Zheng, J. Dong, C.-R. Chang, Y. Chen, X. Hong, J. Luo, S. Wei, W.-X. Li, P. Strasser, Y. Wu, Y. Li, Engineering the electronic structure of single atom Ru sites via compressive strain boosts acidic water oxidation electrocatalysis, Nat. Catal. 2 (2019) 304-313, https://doi.org/10.1038/s41929-019-0246-2.

[13] H. Jin, S. Choi, G.J. Bang, T. Kwon, H.S. Kim, S.J. Lee, Y. Hong, D.W. Lee, H.S. Park, H. Baik, Y. Jung, S.J. Yoo, K. Lee, Safeguarding the RuO_2 phase against lattice oxygen oxidation during acidic water electrooxidation, Energy Environ. Sci. 15 (2022) 1119-1130, https://doi.org/10.1039/d1ee02636d.

[14] Y. Lin, Z. Tian, L. Zhang, J. Ma, Z. Jiang, B.J. Deibert, R. Ge, L. Chen, Chromium-ruthenium oxide solid solution electrocatalyst for highly efficient oxygen evolution reaction in acidic media, Nat. Commun. 10 (2019), 162, https://doi.org/10.1038/s41467-018-08144-3.

[15] J. Su, R. Ge, K. Jiang, Y. Dong, F. Hao, Z. Tian, G. Chen, L. Chen, Assembling Ultrasmall Copper-Doped Ruthenium Oxide Nanocrystals into Hollow Porous Polyhedra: Highly Robust Electrocatalysts for Oxygen Evolution in Acidic Media, Adv. Mater. (2018),

1801351, https://doi.org/10.1002/adma.201801351.

[16] S. Hao, M. Liu, J. Pan, X. Liu, X. Tan, N. Xu, Y. He, L. Lei, X. Zhang, Dopants fixation of Ruthenium for boosting acidic oxygen evolution stability and activity, Nat. Commun. 11 (2020), 5368, https://doi.org/10.1038/s41467-020-19212-y.

[17] N. Wang, S. Ning, X. Yu, D. Chen, Z. Li, J. Xu, H. Meng, D. Zhao, L. Li, Q. Liu, B. Lu, S. Chen, Graphene composites with Ru-RuO_2 heterostructures: Highly efficient Mott–Schottky-type electrocatalysts for pH-universal water splitting and flexible zinc–air batteries, Appl. Catal. B. 302 (2022), 120838, https://doi.org/10.1016/j.apcatb.2021.120838.

[18] J. Wang, Y. Ji, R. Yin, Y. Li, Q. Shao, X. Huang, Transition metal-doped ultrathin RuO2 networked nanowires for efficient overall water splitting across a broad pH range, J. Mater. Chem. A. 7 (2019) 6411-6416, https://doi.org/10.1039/c9ta00598f.

[19] Z.L. Zhao, Q. Wang, X. Huang, Q. Feng, S. Gu, Z. Zhang, H. Xu, L. Zeng, M. Gu, H. Li, Boosting the oxygen evolution reaction using defect-rich ultra-thin ruthenium oxide nanosheets in acidic media, Energy Environ. Sci. 13 (2020) 5143-5151, https://doi.org/10.1039/d0ee01960g.

[20] K. Wang, Y. Wang, B. Yang, Z. Li, X. Qin, Q. Zhang, L. Lei, M. Qiu, G. Wu, Y. Hou, Highly active ruthenium sites stabilized by modulating electron-feeding for sustainable acidic oxygen-evolution electrocatalysis, Energy Environ. Sci. 15 (2022) 2356-2365, https://doi.org/10.1039/d1ee03610f.

[21] X. Cui, P. Ren, C. Ma, J. Zhao, R. Chen, S. Chen, N.P. Rajan, H. Li, L. Yu, Z. Tian, D. Deng, Robust Interface Ru Centers for High-Performance Acidic Oxygen Evolution, Adv. Mater. 32 (2020), 1908126, https://doi.org/10.1002/adma.201908126.

[22] K. Du, L. Zhang, J. Shan, J. Guo, J. Mao, C.C. Yang, C.H. Wang, Z. Hu, T. Ling, Interface engineering breaks both stability and activity limits of RuO_2 for sustainable water oxidation, Nat. Commun. 13 (2022), 5448, https://doi.org/10.1038/s41467-022-33150-x.

[23] B. Zhao, J. Liu, C. Xu, R. Feng, P. Sui, J.-X. Luo, L. Wang, J. Zhang, J.-L. Luo, X.-Z. Fu,

Interfacial engineering of Cu_2Se/Co_3Se_4 multivalent hetero-nanocrystals for energy-efficient electrocatalytic co-generation of value-added chemicals and hydrogen, Appl. Catal. B. 285 (2021), 119800, https://doi.org/10.1016/j.apcatb.2020.119800.

[24] J. Liu, X. Yang, F. Si, B. Zhao, X. Xi, L. Wang, J. Zhang, X.-Z. Fu, J.-L. Luo, Interfacial component coupling effects towards precise heterostructure design for efficient electrocatalytic water splitting, Nano Energy. 103 (2022) 107753, https://doi.org/10.1016/j.nanoen.2022.107753.

[25] L. An, F. Yang, C. Fu, X. Cai, S. Shen, G. Xia, J. Li, Y. Du, L. Luo, J. Zhang, A Functionally Stable RuMn Electrocatalyst for Oxygen Evolution Reaction in Acid, Adv. Funct. Mater. 32 (2022) 2200131, https://doi.org/10.1002/adfm.202200131.

[26] F.J. Kresse G, Efficient iterative schemes for ab initio total-energy calculations using a plane-wave basis set, Phys. Rev. B. 54 (1996) 11169-11186, https://doi.org/10.1103/PhysRevB.54.11169.

[27] F.J. Kresse G, Efficiency of ab-initio total energy calculations for metals and semiconductors using a plane-wave basis set, Comp. Mater. Sci. 6 (1996) 15-50, https://doi.org/10.1016/0927-0256(96)00008-0.

[28] B.K. Perdew JP, Ernzerhof M., Generalized Gradient Approximation Made Simple, Perdew JP, Burke K, Ernzerhof M. 78 (1997), 1396, https://doi.org/10.1103/PhysRevLett.77.3865.

[29] P.E. Blochl, Projector augmented-wave method, Phys Rev B Condens Matter. 50 (1994) 17953-17979, https://doi.org/10.1103/PhysRevB.50.17953.

[30] S. Grimme, J. Antony, S. Ehrlich, H. Krieg, A consistent and accurate ab initio parametrization of density functional dispersion correction (DFT-D) for the 94 elements H-Pu, J Chem Phys. 132 (2010), 154104, https://doi.org/10.1063/1.3382344.

[31] Y. Li, S.H. Chan, Q. Sun, Heterogeneous catalytic conversion of CO_2: a comprehensive theoretical review, Nanoscale. 7 (2015) 8663-8683, https://doi.org/10.1039/C5NR00092K.

[32] S. Chen, H. Huang, P. Jiang, K. Yang, J. Diao, S. Gong, S. Liu, M. Huang, H. Wang, Q. Chen, Mn-Doped RuO_2 Nanocrystals as Highly Active Electrocatalysts for Enhanced Oxygen Evolution in Acidic Media, ACS Catal. 10 (2019) 1152-1160, https://doi.org/10.1021/acscatal.9b04922.

[33] V. Selvanathan, M. Shahinuzzaman, S. Selvanathan, D.K. Sarkar, N. Algethami, H.I. Alkhammash, F.H. Anuar, Z. Zainuddin, M. Aminuzzaman, H. Abdullah, M. Akhtaruzzaman, Phytochemical-Assisted Green Synthesis of Nickel Oxide Nanoparticles for Application as Electrocatalysts in Oxygen Evolution Reaction, Catalysts. 11 (2021), 1523, https://doi.org/10.3390/catal11121523.

[34] A. Ramírez, P. Hillebrand, D. Stellmach, M.M. May, P. Bogdanoff, S. Fiechter, Evaluation of MnO_x, Mn_2O_3, and Mn_3O_4 Electrodeposited Films for the Oxygen Evolution Reaction of Water, J. Phys. Chem. C. 118 (2014) 14073-14081, https://doi.org/10.1021/jp500939d.

[35] A. Ganguly, O. Anjaneyulu, K. Ojha, A.K. Ganguli, Oxide-based nanostructures for photocatalytic and electrocatalytic applications, CrystEngComm. 17 (2015) 8978-9001, https://doi.org/10.1039/C5CE01343G.

[36] F. Ji, Y. Men, J. Wang, Y. Sun, Z. Wang, B. Zhao, X. Tao, G. Xu, Promoting diesel soot combustion efficiency by tailoring the shapes and crystal facets of nanoscale Mn_3O_4, Appl. Catal. B. 242 (2019) 227-237, https://doi.org/10.1016/j.apcatb.2018.09.092.

[37] L. Xu, L. Yang, A. Liu, Facile one-pot synthesis of Mn_3O_4 nanorods and their analytical application, New J. Chem. 45 (2021) 17576-17583, https://doi.org/10.1039/D1NJ02513A.

[38] L. Ai, Y. Wang, Y. Luo, Y. Tian, S. Yang, M. Chen, J. Jiang, Robust interfacial Ru-RuO_2 heterostructures for highly efficient and ultrastable oxygen evolution reaction and overall water splitting in acidic media, J. Alloys Compd. 902 (2022), 163787, https://doi.org/10.1016/j.jallcom.2022.163787.

[39] Q. Feng, Q. Wang, Z. Zhang, Y. Xiong, H. Li, Y. Yao, X.-Z. Yuan, M.C. Williams, M.

Gu, H. Chen, H. Li, H. Wang, Highly active and stable ruthenate pyrochlore for enhanced oxygen evolution reaction in acidic medium electrolysis, Appl. Catal. B. 244 (2019) 494-501, https://doi.org/10.1016/j.apcatb.2018.11.071.

[40] J. Joo, Y. Park, J. Kim, T. Kwon, M. Jun, D. Ahn, H. Baik, J.H. Jang, J.Y. Kim, K. Lee, Mn-Dopant Differentiating the Ru and Ir Oxidation States in Catalytic Oxides Toward Durable Oxygen Evolution Reaction in Acidic Electrolyte, Small Methods. 6 (2022), 2101236, https://doi.org/10.1002/smtd.202101236.

[41] C. Lin, J.-L. Li, X. Li, S. Yang, W. Luo, Y. Zhang, S.-H. Kim, D.-H. Kim, S.S. Shinde, Y.-F. Li, Z.-P. Liu, Z. Jiang, J.-H. Lee, In-situ reconstructed Ru atom array on α-MnO_2 with enhanced performance for acidic water oxidation, Nat. Catal. 4 (2021) 1012-1023, https://doi.org/10.1038/s41929-021-00703-0.

[42] T. He, S. Chen, B. Ni, Y. Gong, Z. Wu, L. Song, L. Gu, W. Hu, X. Wang, Zirconium-Porphyrin-Based Metal-Organic Framework Hollow Nanotubes for Immobilization of Noble-Metal Single Atoms, Angew. Chem. Int. Ed. 57 (2018) 3493-3498, https://doi.org/10.1002/anie.201800817.

[43] B. Zhao, J. Liu, X. Wang, C. Xu, P. Sui, R. Feng, L. Wang, J. Zhang, J.-L. Luo, X.-Z. Fu, CO_2-emission-free electrocatalytic CH_3OH selective upgrading with high productivity at large current densities for energy saved hydrogen co-generation, Nano Energy. 80 (2021) , 105530, https://doi.org/10.1016/j.nanoen.2020.105530.

[44] H. Fei, J. Dong, M.J. Arellano-Jimenez, G. Ye, N. Dong Kim, E.L. Samuel, Z. Peng, Z. Zhu, F. Qin, J. Bao, M.J. Yacaman, P.M. Ajayan, D. Chen, J.M. Tour, Atomic cobalt on nitrogen-doped graphene for hydrogen generation, Nat. Commun. 6 (2015) 8668, https://doi.org/10.1038/ncomms9668.

[45] R. Huang, Y. Wen, H. Peng, B. Zhang, Improved kinetics of OER on Ru-Pb binary electrocatalyst by decoupling proton-electron transfer, Chinese J. Catal. 43 (2022) 130-138, https://doi.org/10.1016/S1872-2067(21)63856-1.

[46] B. Zhao, J.-W. Liu, Y.-R. Yin, D. Wu, J.-L. Luo, X.-Z. Fu, Carbon nanofibers@NiSe core/sheath nanostructures as efficient electrocatalysts for integrating highly selective methanol conversion and less-energy intensive hydrogen production, J. Mater. Chem. A. 7 (2019) 25878-25886, https://doi.org/10.1039/c9ta09782a.

[47] Y. Qi, Y. Zhang, L. Yang, Y. Zhao, Y. Zhu, H. Jiang, C. Li, Insights into the activity of nickel boride/nickel heterostructures for efficient methanol electrooxidation, Nat. Commun. 13 (2022) 4602, https://doi.org/10.1038/s41467-022-32443-5.

[48] L. Hu, X. Zeng, X. Wei, H. Wang, Y. Wu, W. Gu, L. Shi, C. Zhu, Interface engineering for enhancing electrocatalytic oxygen evolution of NiFe LDH/NiTe heterostructures, Appl. Catal. B. 273 (2020), 119014, https://doi.org/10.1016/j.apcatb.2020.119014.

[49] Y. Jiang, H. Liu, Y. Jiang, Y. Mao, W. Shen, M. Li, R. He, Adjustable heterointerface-vacancy enhancement effect in RuO_2@Co_3O_4 electrocatalysts for efficient overall water splitting, Appl. Catal. B. 324 (2023), 122294, https://doi.org/10.1016/j.apcatb.2022.122294.

[50] M. Etzi Coller Pascuzzi, A. Goryachev, J.P. Hofmann, E.J.M. Hensen, Mn promotion of rutile TiO_2-RuO_2 anodes for water oxidation in acidic media, Appl. Catal. B. 261 (2020), 118225, https://doi.org/10.1016/j.apcatb.2019.118225.

[51] Y. Zhao, J. Hu, C.-L. Chiang, Y. Li, W. Yang, Z. Yang, W.-H. Hung, Y.-G. Lin, Z. Chen, B. Li, P. Gao, H. Li, Ruthenium oxychloride supported by manganese oxide for stable oxygen evolution in acidic media, J. Mater. Chem. A. 10 (2022) 20964-20974, https://doi.org/10.1039/d2ta05335g.

[52] C.F.D. Linsey C. Seitz, Kazunori Nishio, Yasuyuki Hikita,, A.D. Joseph Montoya, Charlotte Kirk,Aleksandra Vojvodic,, J.K.N. Harold Y. Hwang, Thomas F. Jaramillo, A highly active and stable $IrO_x$$SrIrO_3$ catalyst for the oxygen evolution reaction, Science. 353 (2016) 1011–1014, https://www.science.org/doi/10.1126/science.aaf5050.

[53] L. Li, G. Zhang, J. Xu, H. He, B. Wang, Z. Yang, S. Yang, Optimizing the Electronic Structure of Ruthenium Oxide by Neodymium Doping for Enhanced Acidic Oxygen

Evolution Catalysis, Adv. Funct. Mater. 33 (2023), 2213304, https://doi.org/10.1002/adfm.202213304.

[54] W. Sun, Y. Song, X.-Q. Gong, L.-m. Cao, J. Yang, An efficiently tuned d-orbital occupation of IrO_2 by doping with Cu for enhancing the oxygen evolution reaction activity, Chemical Science. 6 (2015) 4993-4999, https://doi.org/10.1039/C5SC01251A.

[55] L. Giordano, B. Han, M. Risch, W.T. Hong, R.R. Rao, K.A. Stoerzinger, Y. Shao-Horn, pH dependence of OER activity of oxides: Current and future perspectives, Catal. Today. 262 (2016) 2-10, http://dx.doi.org/10.1016/j.cattod.2015.10.006.

[56] J. Rossmeisl, Z.W. Qu, H. Zhu, G.J. Kroes, J.K. Nørskov, Electrolysis of water on oxide surfaces, J. Electroanal. Chem. 607 (2007) 83-89, https://doi.org/10.1016/j.jelechem.2006.11.008.

[57] H.B. Tao, Y. Xu, X. Huang, J. Chen, L. Pei, J. Zhang, J.G. Chen, B. Liu, A General Method to Probe Oxygen Evolution Intermediates at Operating Conditions, Joule. 3 (2019) 1498-1509, https://doi.org/10.1016/j.joule.2019.03.012.

[58] X. Wang, X. Wan, X. Qin, C. Chen, X. Qian, Y. Guo, Q. Xu, W.-B. Cai, H. Yang, K. Jiang, Electronic Structure Modulation of RuO_2 by TiO_2 Enriched with Oxygen Vacancies to Boost Acidic O_2 Evolution, ACS Catal. 12 (2022) 9437-9445, https://doi.org/10.1021/acscatal.2c01944.

[59] H. Jin, X. Liu, P. An, C. Tang, H. Yu, Q. Zhang, H.J. Peng, L. Gu, Y. Zheng, T. Song, K. Davey, U. Paik, J. Dong, S.Z. Qiao, Dynamic rhenium dopant boosts ruthenium oxide for durable oxygen evolution, Nat. Commun. 14 (2023) 354, https://doi.org/10.1038/s41467-019-12886-z.

[60] V. Stamenkovic, B.S. Mun, K.J.J. Mayrhofer, P.N. Ross, N.M. Markovic, J. Rossmeisl, J. Greeley, J.K. Nørskov, Changing the Activity of Electrocatalysts for Oxygen Reduction by Tuning the Surface Electronic Structure, Angew. Chem. Int. Ed. 118 (2006) 2963-2967, https://doi.org/10.1002/ange.200504386.

[61] S. Niu, X.-P. Kong, S. Li, Y. Zhang, J. Wu, W. Zhao, P. Xu, Low Ru loading $RuO_2/(Co,Mn)_3O_4$ nanocomposite with modulated electronic structure for efficient oxygen evolution reaction in acid, Appl. Catal. B. 297 (2021), 120442, https://doi.org/10.1016/j.apcatb.2021.120442.